Programmable Droplet Transport on Multi-Bioinspired Slippery Surface with Tridirectionally Anisotropic Wettability

Zexin Cai[a], Faze Chen[a,b,*], Yanling Tian[a,b,c], Dawei Zhang[a,b], Zhongxu Lian[d,*], Moyuan Cao[e,f,*]

[a] School of Mechanical Engineering, Tianjin University, Tianjin 300350, China

[b] Key Laboratory of Mechanism Theory and Equipment Design of Ministry of Education, Tianjin University, Tianjin 300350, China

[c] School of Engineering, University of Warwick, Coventry CV4 7DL, UK

[d] Key Laboratory for Cross-Scale Micro and Nano Manufacturing of Ministry of Education, Changchun University of Science and Technology, Changchun 130022, China

[e] School of Materials Science and Engineering, Nankai University, Tianjin 300350, P. R. China

[f] Haihe Laboratory of Sustainable Chemical Transformations, Tianjin 300192, P. R. China

*Corresponding author. E-mail addresses: faze.chen@tju.edu.cn (Faze Chen), lianzhongxu@cust.edu.cn (Zhongxu Lian), moyuan.cao@tju.edu.cn (Moyuan Cao).

Abstract: Directional droplet transport on functional surfaces with anisotropic wettability has shown great potential applications in various fields such as water harvesting, chemical micro-reaction, and biomedical analysis. However, the in-plane manipulation of the anisotropic droplet motion in more than two directions is still a challenge. Herein, through the fusion of inspirations from rice leaves, butterfly wings and Pitcher plants, we report a tridirectionally anisotropic slippery surface (TASS) with periodic step-like micro grooves for programmable droplet transport. TASS possesses a tridirectional droplet sliding behavior, *i.e.*, the ultra-slipperiness along the grooves with a sliding angle of ~2°, and the bidirectionally anisotropic sliding perpendicular to the grooves with sliding angle difference up to ~50°, which is caused by the pinning effect of the step edge. Under the

assistance of periodic vertical vibration, groove-features and droplet-volume dependent unidirectional droplets transports are realized on horizontally placed TASS, based on which two micro-reactors are designed to control the sequence of droplets merging and subsequent chemical reactions. Additionally, by utilizing the slipperiness (*i.e.*, ultra-low sliding angle for liquid droplet) along the grooves simultaneously, programmable droplet transport under vertical vibration is further demonstrated on a tilted TASS. This work will provide a new avenue for the understanding of anisotropic wettability on asymmetric slippery surface, and thus offer a great opportunity to develop advanced interface for multidirectional droplet transport, chemical micro-reactor, *etc*.

Keywords: Droplet transport, bioinspired, tridirectional anisotropy, slippery surface, vibration

1. Introduction

Droplet transports on functional interfaces with anisotropic wettability have drawn keen yet continuously increasing research interest from academic communities due to their great potential applications in water purification/collection [1], [2], [3], [4], chemical micro-reactor [5], [6], [7], biomedical analysis [8], [9], [10] and so on. A common method for droplet transport is to design non-uniformly wettable surfaces with chemical and/or topographical gradients, such as superhydrophobic-superhydrophilic patterns [11], [12], [13], wedge-shaped structures [14], [15], [16], [17], lubricant meniscus [18], [19], *etc*. Although these passive strategies are always free of external energy input, it is difficult to realize continuous and on-demand droplet transport. To address these problems, various external fields, such as electric [20], [21], [22], [23], thermal [24], [25], [26], and magnetic [27], [28], [29], [30] have been introduced to provide extra driving force for continuous and programmable droplet transport. However, electric field induced wettability gradient always depends on non-uniform charge accumulation on dielectric materials, which greatly limits its application scope; thermal actuation creates contrast wettability *via* localized temperature gradient, which is unsuitable

for those heat-sensitive substrates and liquids in some scenarios (*e.g.*, biomedical detection and analysis); magnetic stimulation is restricted to substrates and/or liquids with magnetic response, and doping the substrates and/or droplets with magnetic particles is often-employed, but it requires the substrates to be flexible and may introduce undesired contamination to the droplets. By contrast, mechanical vibration shows considerable advantages for assisted droplet manipulation, such as broad substrate applicability, no cross-contamination, and easy-to-operate. Generally, based on the cardinal direction relations between the vibration and substrate surface, two kinds of mechanical vibration can be used to drive droplet transport. One is horizontal vibration that imparts the substrate with periodic horizontal movement, creating friction force on the droplet and thereby driving it to move [31], [32]. The other one is vertical vibration, by which inhomogeneous deformation of the droplet can be formed and thereafter unidirectional motion is realized [33], [34]. For both of the mechanical vibrations, anisotropic wettability of the underlying surface is the basic condition to trigger unidirectional droplet movement.

Nature provides plentiful functional surfaces with anisotropic wettability. For example, the rice leaves have bi-directionally anisotropic wettability, which enables water droplets to roll along the leaf veins to the roots and significantly improves the survival of rice during drought [35], [36], [37]. The butterfly can fly freely in the rain due to the unidirectional wetting properties of its wings, upon which water droplets only roll down radially outward from the wings without wetting the body [38], [39]. The peristome of *Nepenthes* Pitcher plants can transport liquids directionally to form a slippery surface, which helps Pitcher plants to capture insects [40], [41], [42], [43]. By mimicking these natural surfaces, various artificial functional interfaces with anisotropic wetting properties have been prepared, such as lotus leaf-inspired superhydrophobic surfaces [44], [45], [46], [47] and the *Nepenthes*-inspired slippery liquid-infused surfaces (SLISs) [48], [49], [50]. Generally, the excellent

water mobility of superhydrophobic surface makes it difficult for water droplets to stay on the surface, thus the dynamic behavior of water droplet is sometimes difficult to be controlled. In addition, the unstable air cushions locked in the micro/nano structures are prone to collapse under rough situations (*e.g.*, high-pressure or high-humidity), resulting in an irreversible conversion of the droplet from Cassie state to Wenzel state [49], [51], which is undesired for flexible droplet manipulation. Different from the superhydrophobic surface, SLIS provides a flexible and versatile platform for transport of various liquid droplets due to the lubricant injection. On one hand, the lubricant layer guarantees the excellent repellence towards various liquids with low contact angle hysteresis. On the other hand, the large adhesion force between the droplets and SLIS prevents the droplets from detaching from the surface, which enhances the controllability of the droplet behavior. Thus, the SLIS with anisotropic wettability has been widely used in the fields of droplet transport. For example, inspired by the wetting properties of Pitcher plants and rice leaves, Dai *et al*. prepared a SLIS that consisted of liquid-infused nanotextures on regular microgrooves, the topographical anisotropy endowed the SLIS with capacities of directional droplet transport and enhanced water harvesting [52]. Under similar inspiration, Li *et al*. fabricated an integrated mesh with orthogonal anisotropic slippery tracks and realized unidirectional permeation of droplets [53]. Additionally, by integrating the wedge-shaped structures of shore bird beak with SLIS, Yang *et al*. realized directional and self-driven transport of droplets [54]. These works have well addressed the preparation of SLISs with bidirectionally anisotropic wettability, and several potential applications based on liquid manipulation have also been demonstrated on lab-scale. However, the bidirectional SLISs could only control the motion of droplets in two directions, thereby limiting their versatility and functionality. Therefore, it is urgently needed to develop an advanced SLIS with multidirectionally anisotropic wettability that can manipulate droplet transport in more than two directions.

Herein, we report a multi-bioinspired tridirectionally anisotropic slippery surface (TASS) *via* rationally integrating the bidirectional anisotropy of rice leaves, the unidirectional wettability of butterfly wings, and the slippery property of Pitcher plants. The designed periodic step-like micro grooves are demonstrated to be crucial for the tridirectional anisotropy owning to the pinning effect caused by the boundaries of the steps. Under the assistance of periodic vertical vibration, unidirectional droplet transports along the two directions that are perpendicular to the grooves are realized on a horizontally placed TASS, and two micro-reactors are further designed by changing the heights of steps and the volume of droplets. In addition, multidirectional droplet transports on a tilted TASS are also demonstrated by using gravity and vertical vibration as driving sources. In comparison with the previous publications, this work describes a multi-bioinspired strategy to construct SLIS with multidirectionally anisotropic wettability, and thereby opens a new avenue for programmable droplet transport in more than two directions.

2. Materials and Methods

2.1 Materials

Copper sheets ($10 \times 10 \times 0.5$ mm^3) were purchased from Lingbang Hardware Technology Co., Ltd. (Jiangsu, China). Sodium hydroxide (NaOH), copper chloride ($CuCl_2$), and ammonium persulfate [$(NH_4)_2S_2O_4$] were purchased from Kemate Chemical Technology Co., Ltd. (Tianjin, China), and hydrochloric acid (HCl) was purchased from Jiangtian Chemical Technology Co., Ltd. (Tianjin, China). Silicone oil (viscosity ~100 cSt at 25 °C) was supplied by Tianying Industry and Trade Co., Ltd. (Guangdong, China), and 1*H*,1*H*,2*H*,2*H*-Perfluorododecyltrichlorosilane [FAS, $CF_3(CF_2)_9CH_2CH_2SiCl_3$] was obtained from TITAN Technology Co., Ltd. (Shanghai, China). Simulated body fluid (SBF) was obtained from Phygene Life Sciences Company (Fujian, China). All chemicals are analytically pure and were used as provided without extra purification.

2.2 Fabrication of TASS

TASS was designed from the bio-inspiration of the bidirectional anisotropy of rice leaves, the unidirectional wettability of butterfly wings, and the slippery surface of Pitcher plants (Figure 1a). The specific preparation process of TASS is shown in Figure 1b. Periodical step-like micro grooves on the polished copper substrate were fabricated by two-round femtosecond laser line-by-line ablation (FemtoYL-40, China, 1034 nm, 340 fs). The ablation parameters were set to be: line interval = 10 μm, scanning speed = 800 mm/s, frequency = 100 kHz, average power = 4.85 W. *L* (140-320 μm) and *W* (80-170 μm) indicated the width and interval of each complete microgroove, respectively. The height of micro grooves was adjusted by the scanning number (SN) of the laser beam, which varied from 10 to 50 but kept the same for the first and second round laser ablation to fabricate the step-like micro grooves.

Laser ablated samples were then ultrasonically washed with hydrochloric acid (1 mol/L) and deionized water in sequence for 5 min to remove the oxide layer formed during laser ablation. The cleaned samples were then immersed into an aqueous solution of 2.5 mol/L NaOH and 0.15 mol/L $(NH_4)_2S_2O_8$ for 5 min at room temperature to generate nano structures on their surfaces. After rinsing with deionized water and drying, the samples with step-like micro/nano hierarchical structures were immersed into fluorosilane ethanol solution for 1 h to lower surface energy. Subsequently, the samples were immersed in silicone oil for 1 h to realize complete lubricant infusion. After taking out, the extra lubricant on the samples was removed by high-speed spin coating with a spin coater (KW-4A, China) to obtain a conformal lubricant film. In addition, as illustrated in Figure 1c, the sliding angles (SAs) of droplets moving along the surface in three directions (*i.e.*, “up” the steps, “down” the steps, and parallel to the grooves) were defined as SA_{up}, SA_{down} and $SA_{//}$, respectively.

2.3 Sample Characterization

The 3D profile of the sample was observed through a laser confocal microscope (LSM 700, ZEISS, German). The surface morphologies of the samples were characterized by using a scanning electron microscope (SEM, Quanta FEG 250, FEI, America). The crystal structure and elements of the surface were characterized by X-ray diffraction (XRD, D8 Advance, Bruker, German) and energy-dispersive spectroscopy (EDS, X-Max, Oxford, England), respectively. Static contact angles (CAs) and dynamic sliding angles (SAs) were measured by an optical contact angle meter (SZ-CAMC33, Sunzern, China) at room temperature with a 7 μL droplet. In order to ensure the accuracy of the results, five positions were randomly selected for each sample to measure, and their average values were reported herein.

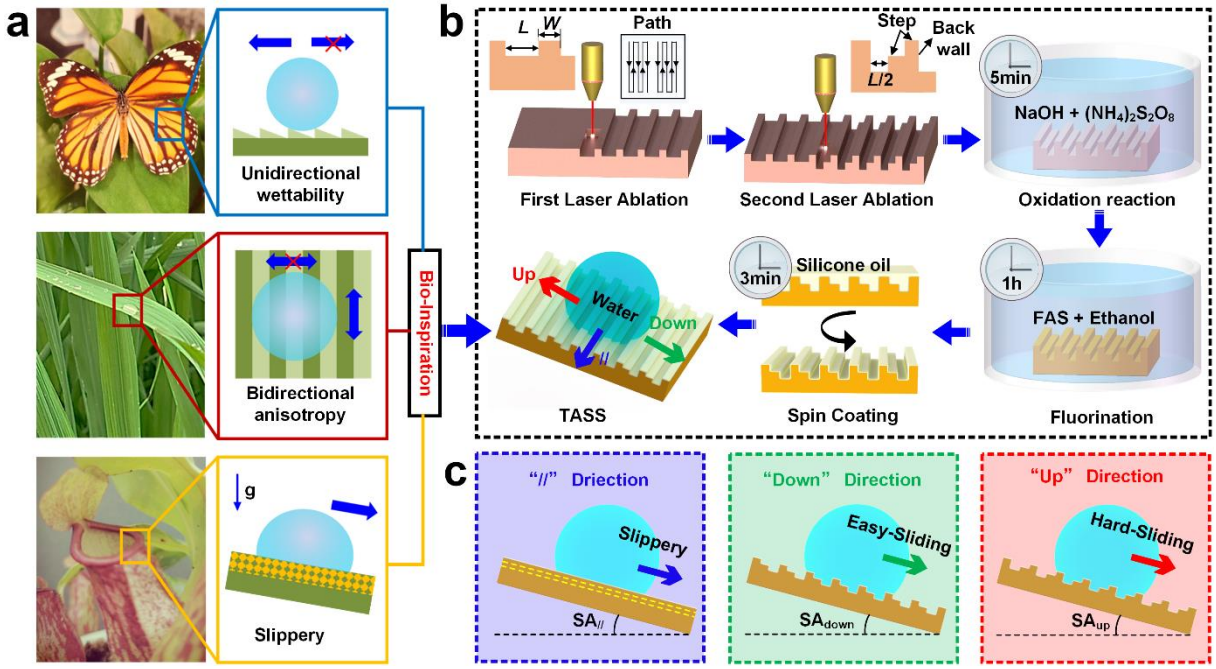

Figure 1. Schematic illustration of the fabrication of multi-bioinspired TASS. a) Bio-inspiration of the unidirectional wettability of butterfly wings, the bidirectional anisotropy of rice leaf, and the slippery surface of Pitcher plant. b) Fabrication of TASS by femtosecond laser ablation, chemical oxidation, and subsequent lubricant infusion. c) Illustration of the tridirectional anisotropy (*i.e.*, the "//", "down" and "up" directions) of the TASS.

2.4 Mechanical Vibration Driven Droplet Transport on TASS

TASS was fixed on an electrodynamic vibration generator (VT-150, Sushi, China) and the testing

liquid droplet was pre-deposited on TASS by a syringe. Then the sample was vibrated vertically under a sinusoidal signal applied by a signal generator. The vibration amplitude could be adjusted among 0~10 Vpp, and the frequency varied from 30 to 50 Hz. The motion of the droplet was captured by a digital camera, and the critical amplitude (U_{CA}) of the mechanical vibration to initiate the movement of the droplet was recorded. Each U_{CA} was measured 5 times and the average value was reported herein.

3. Result and Discussion

3.1 Fabrication and Characterization of the TASS

Figure 2a shows the surface morphologies of the two-round femtosecond laser ablated copper sheet (SN = 20). It could be seen that periodically directional step-like grooves covered with rough crater structures were created on the copper sheet, and the inserted SEM cross-sectional view verified that the height of each step structure was relatively uniform. 3D confocal microscopy image (Figure 2d) and its cross-section profile (Figure 2c) show that the heights of the middle (h_1) and bottom (h_2) steps were 17.7 ± 1.8 μm and 33.8 ± 1.2 μm, respectively. The heights of the steps could be well adjusted by changing the SN. The changes in the heights were almost linear with increased SN, as shown in Figure 2d, when the SN increased from 10 to 50, h_1 changed from 7.5 ± 1.1 μm to 44.2 ± 2.5 μm, and h_2 increased from 16.2 ± 0.9 μm to 85.4 ± 2.3 μm. Moreover, it could be seen that $h_2 \approx 2h_1$, which indicated that the groove with similar height was constructed during each round of femtosecond laser ablation. The majority of the reported samples in this paper were ablated with the SN of 20 unless specified otherwise. After NaOH-assisted chemical oxidation, the surface of the sample was uniformly covered with a large number of micro-scale particles and needle-like nano-spikes (Figure 2e). The comparison of the XRD spectra shows that several diffraction peaks of $Cu(OH)_2$ planes

(JCPDS card No. 80-0656) appeared on the oxidized sample (Figure S1, Supporting Information), indicating that the compositions of the formed particles and spikes were $Cu(OH)_2$ [55]. After subsequent fluorination, F-containing groups were anchored on the surface (Figure S2, Supporting Information), enabling the surface to be super water repellent, but remarkably, the anisotropy of the superhydrophobicity was almost negligible (Figure S3, Supporting Information). As the SN increased from 10 to 50, the max differences of CAs and SAs in the three directions (*i.e.*, the "//", "down" and "up" directions) of each sample were only ~2.7° and ~2.0°, respectively. Additionally, the CAs and SAs in the "up" and "down" directions were almost the same, showing negligible wettability anisotropy of the superhydrophobic surfaces. Therefore, the resultant superhydrophobic surfaces with step-like micro grooves were not suitable for multidirectional manipulation of water droplets.

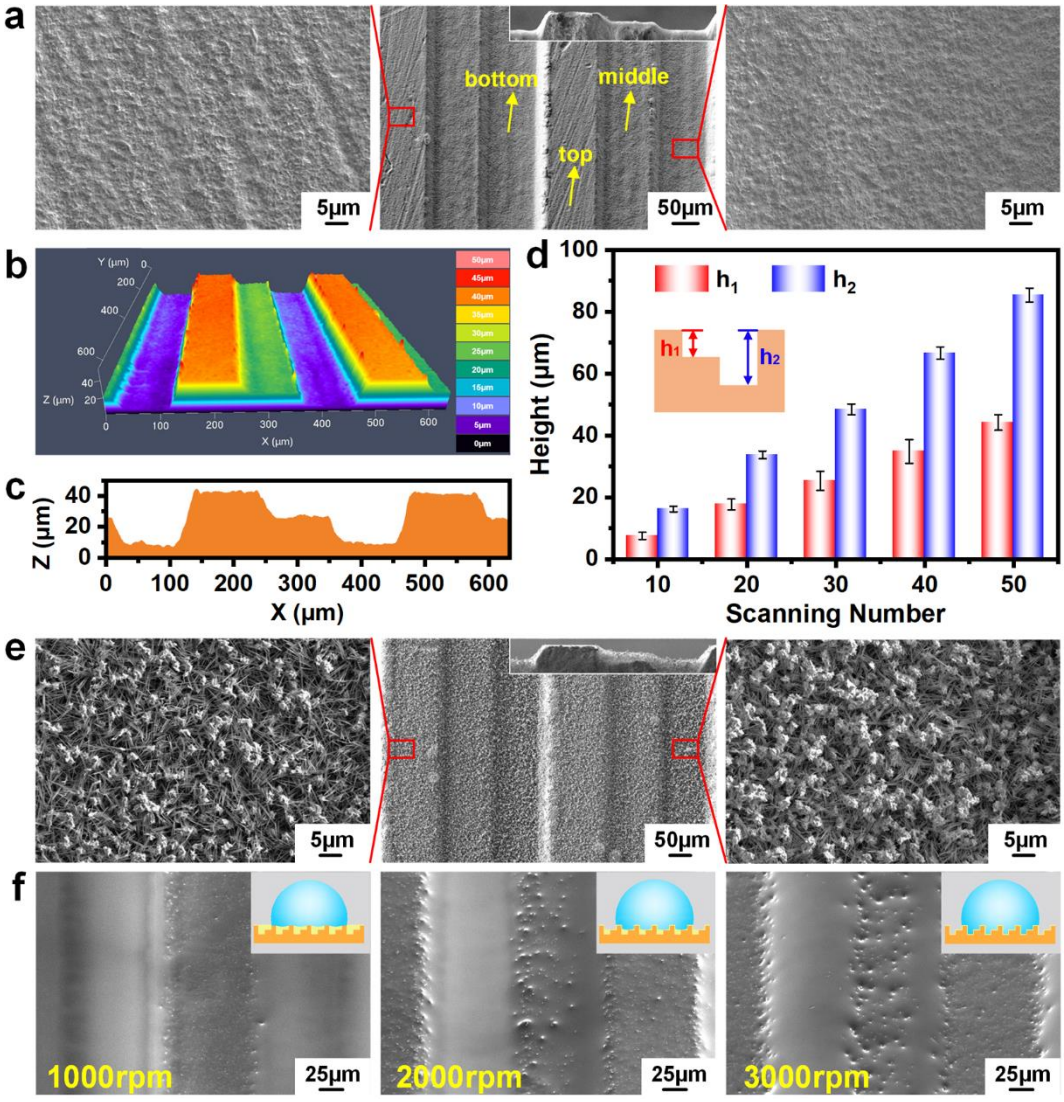

Figure 2. a) SEM images of the laser ablated step-like structures. The inset shows the cross-sectional morphology of the steps. b) 3D topography and c) cross-section profile of the laser ablated surface. d) Relationship between the height of laser ablated steps and SN. e) SEM images of the laser ablated steps after chemical oxidation and fluorination. The inset shows the corresponding cross-sectional view of the steps. f) Lubricant distribution of the slippery surface prepared under different spinning speeds. The insets illustrate the cross-sectional diagram of water droplets on the slippery surfaces from the "//" directions of the engineered steps.

Subsequently, the fluorinated samples were infused with silicone oil to prepare slippery surfaces. It was demonstrated that spinning speed has an obvious influence on the lubricant distribution of the resultant slippery surface [56], [57], so slippery surfaces were prepared under different spinning speeds and then tested. As shown in Figure 2f, as the spinning speed was increased from 1000 rpm to 3000 rpm, more silicone oil was removed during the spin-coating process, which enhanced the visibility of the underlying micro/nano structures. However, a conformal oil film was always retained on the surface even under the spinning speed of 5000 rpm (Figure S4, Supporting Information), which could be attributed to the nanostructures generated capillary forces that enhanced the retention of lubricant. Owing to the difference in lubricant distribution, the resulting slippery surfaces exhibited different contact states with droplets (insets in Figure 2f) and thereby dissimilar wettability (Figure S5, Supporting Information). When the spinning speed was 1000 rpm, only the top surface of the steps was exposed while the grooves were filled with oil, the water sliding angles (SAs) were $SA_{up} = 2.3 \pm 0.3°$, $SA_{down} = 2.2 \pm 1.0°$, and $SA_{//} = 1.1 \pm 0.2°$, demonstrating excellent adhesion resistance to water droplet along the surface [58] and negligible anisotropy between the parallel and vertical directions. For the sample treated at the spinning speed of 2000 rpm, the oil in the grooves was partially removed while the bottom surfaces were still fully covered with a lubricant layer,

making part of the droplet stuck in the grooves, and much bigger SAs in the vertical directions (SA_{up} = 16.9 ± 1.3°, SA_{down} = 13.3 ± 0.5°) than that in the parallel direction ($SA_{//}$ = 2.0 ± 0.6°) were observed. When the spinning speed was further increased to 3000 rpm, most oils in the micro grooves were removed except those locked in the nanostructures, endowing the slippery surface with remarkable tridirectional anisotropy (SA_{up} = 27.0 ± 2.1°, SA_{down} = 16.3 ± 0.6°, $SA_{//}$ = 1.8 ± 0.6°). Furthermore, when the speed reached 5000 rpm, the SA_{up}, SA_{down} and $SA_{//}$ were respectively measured to be 64.4 ± 2.7°, 25.0 ± 1.8°, and 6.9 ± 0.7°. Therefore, the similar SAs in the parallel direction (*i.e.*, $SA_{//}$) of these samples further demonstrated that the nano structures on the surfaces could effectively prevent the loss of lubricant during the spin-coating process. Additionally, the difference between SA_{up} and SA_{down} verified the feasibility to obtain directional anisotropy in the vertical directions *via* the micro grooves and lubricant distribution. Although higher spinning speed resulted in more significant tridirectional anisotropy (Figure S5, Supporting Information), by considering the retention of the oil layer and durability of the slippery surface, a spinning speed of 3000 rpm was selected to prepare the TASS in the following parts of this paper.

3.2 Static CA of Droplet on TASS

The height (*i.e.*, SN) and period (including *L* and *W*) of the step-like grooves affected the static CA of water droplet on the TASS (Figure S6, Supporting Information). The testing droplet could completely fill the rough step-like grooves of TASS and fully contact with the lubricant. In the "//" direction, the lubricant film could be regarded as a smooth and flat substrate, indicating a free spreading of the droplet along this direction. Consequently, the CA in the "//" direction ($CA_{//}$) could be described by Young's equation [59]:

$$\gamma_{LA}\cos\theta_{//} = \gamma_{OA} - \gamma_{OL} \quad (1)$$

where $\theta_{//}$, γ_{OA}, γ_{OL}, and γ_{LA} represented the Young's CA in the "//" direction (*i.e.*, $CA_{//}$), the interfacial

tensions of oil-air (~20 mN/m), oil-water (~38 mN/m), and water-air (~72 mN/m), respectively. The calculated $\theta_{//}$ (104.5°) was close to the experimentally measured $CA_{//}$ (105.4 ± 0.9°) that was independent of the SN and period of the TASS. By contrast, the spreading of droplet along with the "up" and "down" directions were significantly impeded by the step-like grooves due to the pinning effect of the edge [60], [61], making the measured CA_{up} and CA_{down} much larger than $CA_{//}$. According to the drop shape analysis by the $\theta/2$ method [62], CA can be calculated by using the following equation:

$$\theta = 2\arctan(2H / l) \quad (2)$$

where θ, H, and l denoted CA, height and length of the contact line of the deposited droplet, respectively. It could be seen from Figure S6b (Supporting Information) that as the SN increased from 10 to 50, the CAs of droplets in the "up" direction (CA_{up}) changed from 110.7 ± 1.9° to 135.9 ± 0.7°, and that in the "down" direction (CA_{down}) increased from 110.4 ± 1.2° to 134.7 ± 0.5°, indicating that the hydrophobicity in the vertical directions of the TASS was enhanced *via* the micro grooves. When the heights of steps increased (the SN increased from 10 to 50), the number of grooves (N_g) covered by the droplet decreased from 7 to 4 (Table S1, Supporting Information), which resulted in a significant decrease of l in the vertical direction ($l_\perp$) (from 2.48 mm to 1.83 mm) and a slight increase of H (from 1.60 mm to 1.71 mm) (Figure S6c, Supporting Information). Therefore, the SN (*i.e.*, the height of the steps) ultimately changed the ratio of H to l (Figure S6d, Supporting Information), and thereby influenced the CA values of the TASS according to Equation (2).

The period of the step-like grooves is another critical structure parameter of the TASS, which, however, had little effect on the hydrophobicity of TASS (Figure S6e, Supporting Information). When the period was small (220-310 μm), N_g decreased by 1 for every 30 μm incensement in the period (Table S2, Supporting Information), H and $l_\perp$ retained nearly constant (Figure S6f, Supporting

Information), corresponding to the almost unchanged CAs. For the TASS with a period larger than 340 μm, fluctuation of CA resulting from the difference in droplet pinning state was observed. As illustrated in Figure S6h (Supporting Information), when the period increased initially, $l_{\perp}$ gradually increased while N_g retained constant, indicating that H reduced and thereby the CA decreased. Once CA decreased to a critical value with certain periods (*e.g.*, 370 μm and 430 μm here), the droplet would be pinned to the grooves with N_g decreased by 1, and the corresponding $l_{\perp}$ decreased abruptly while H increased, the CA would thereby increase again. Therefore, for a droplet with a given volume, its CA on the TASS would fluctuate with the change of groove period.

3.3 SA of Droplet on TASS

As shown in Figure 3a-c and Video S1 (Supporting Information), the TASS (SN = 20, period = 340 μm, spinning speed = 3000 rpm) showed remarkable tridirectional anisotropy (*i.e.*, the "//", "down", and "up" directions) in terms of water droplet (7 μL) sliding. The SAs of water droplets on the TASS were measured to be $SA_{//} = 1.8 \pm 0.6°$, $SA_{down} = 17.0 \pm 0.7°$, and $SA_{up} = 27.4 \pm 1.9°$, respectively, and it was also demonstrated that the sliding resistance along the "//" direction was the lowest while that along the "up" direction was the highest. During the sliding process, the resistance to the droplet ($F_{resistance}$) could be calculated by the simplified Furmidge equation [63], [64], [65]:

$$F_{resistance} = \gamma l(\cos\theta_r - \cos\theta_a) \quad (3)$$

where γ was the surface energy of water, θ_r and θ_a respectively represented the receding and advancing CAs of the water droplet. In the "//" direction, the droplet motion was affected by the frictional resistance from lubricant film, so the $F_{resistance}$ was mainly determined by the contact area between the droplet and TASS. By contrast, in the "down" and "up" directions, the droplet sliding was significantly inhibited by the step-like micro grooves, and the $F_{resistance}$ was composed of the pinning force at the step edge, the adhesion force at the step and back wall, and the resistance from the

underlying steps. Therefore, the $F_{resistance}$ along the "down" and "up" directions were much larger than that along the "//" direction, which was also verified by the measurement of θ_r and θ_a along the three directions (Figure S7, Supporting Information) according to Equation (3).

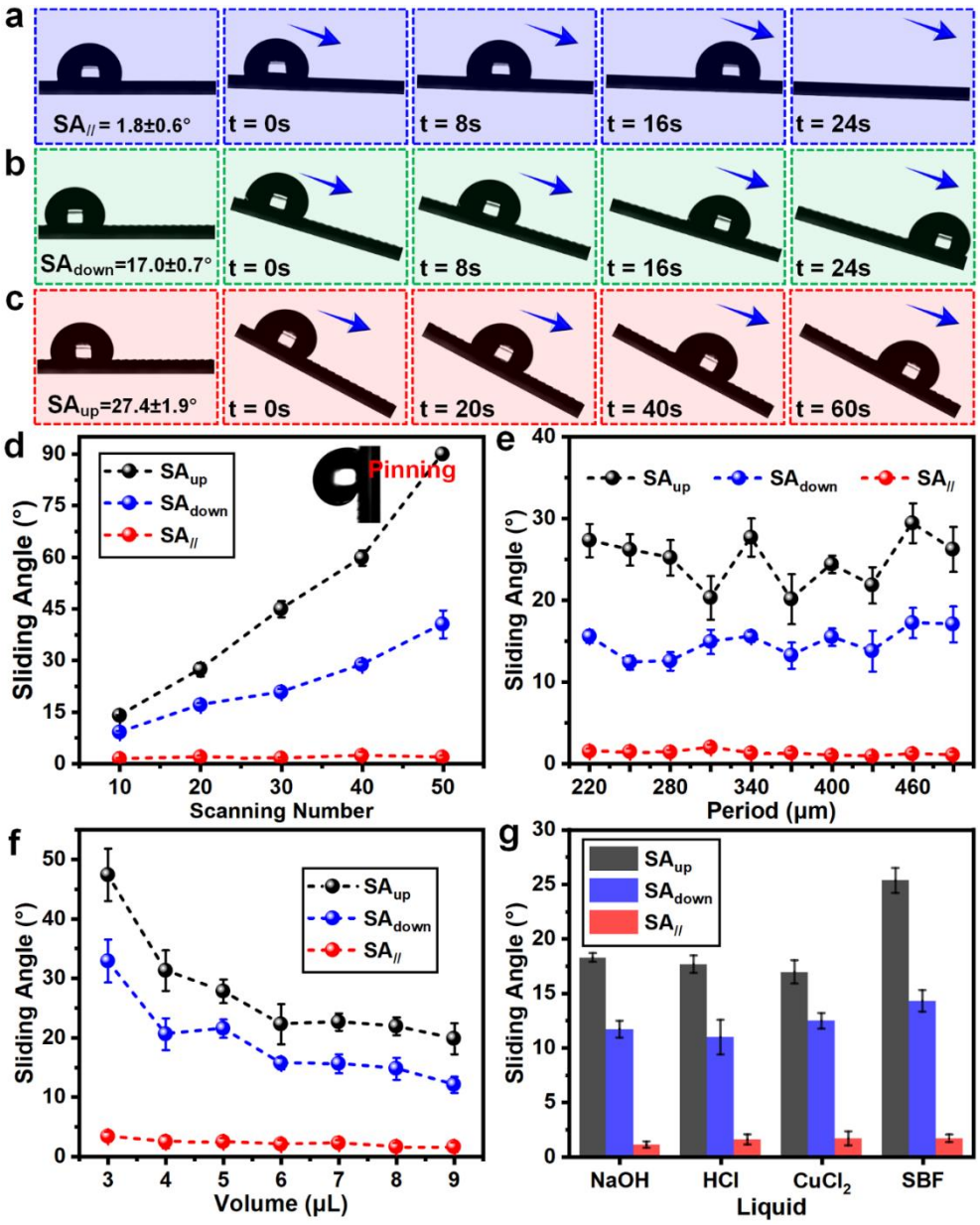

Figure 3. Sliding of 7 μL water droplet on the TASS along the a) "//", b) "down" and c) "up" directions. The influence of d) SN and e) period on SA of the TASS. SA of f) water droplet with different volume and g) different kinds of liquids, including NaOH (pH = 14), HCl (pH = 1), $CuCl_2$ (1 mol/L) and SBF.

The driving force of the droplet ($F_{driving}$) during sliding was provided by the component of gravity,

290 which could be expressed as:

291 $$F_{\text{driving}} = \rho g V \sin\alpha \quad (4)$$

292 where ρ, V, g, α represented water density, volume, gravitational acceleration and tilt angle of the
293 surface (*i.e.*, SA), respectively. When the TASS was gradually tilted to meet $F_{\text{driving}} > F_{\text{resistance}}$, the
294 droplet started to slide on the surface, and the corresponding SAs of droplets on TASSs could be
295 measured. As shown in Figure 3d, the TASS prepared under the SN of 10 exhibited tridirectional
296 anisotropy with $SA_{//} = 1.3 \pm 0.4°$, $SA_{down} = 9.0 \pm 0.6°$ and $SA_{up} = 13.9 \pm 0.3°$. When the SN was
297 increased to 50, $SA_{//}$ retained stable at ~2°, while SA_{down} and SA_{up} respectively increased to 40.5 ± 4.0°
298 and 90° (*i.e.*, the droplet was pinned), demonstrating enhanced tridirectional anisotropy of the TASS.
299 As depicted in Figure 3e, as the period increased from 220 μm to 490 μm, the SAs in the three
300 directions did not show obvious change but fluctuated around a relatively stable value (~2°, ~15° and
301 ~25° in the "//", "down" and "up" directions, respectively). The critical points of the SAs fluctuation
302 were almost the same as those of the CAs (Figure S6e-h, Supporting Information), which indicated
303 that the initial pinning state of the deposited droplet also influenced the subsequent sliding. In addition,
304 the volume of the droplet also had an obvious effect on its tridirectionally anisotropic sliding. As can
305 be seen from Figure 3f, the SAs in the three directions all decreased as the volume of the droplet
306 increased from 3 μL to 9 μL, especially the SA_{down} changed from 32.9 ± 3.6° to 12.1 ± 1.4°, and the
307 SA_{up} decreased from 47.4 ± 4.4° to 19.8 ± 2.6°. This could be attributed to the fact that the droplet
308 with a larger volume generated a greater driving force (F_{driving}) during sliding (Equation (4)) [66].
309 Meanwhile, the excellent liquid repellency of TASS was durable towards various complex aqueous
310 solutions (Figure 3g). Owing to the higher density of HCl, NaOH and $CuCl_2$ than water, their
311 corresponding droplets exhibited slightly lower SAs (especially the SA_{down} and SA_{up}) on the TASS.
312 By contrast, SBF droplet showed a little higher SAs since its higher viscosity contributed to the

increase of frictional resistance ($F_{resistance}$) during sliding. These results demonstrated that the TASS could be used for the manipulation of various complex liquids.

3.4 Mechanism of Tridirectionally Anisotropic Sliding

To further investigate the mechanism of tridirectional anisotropy of TASS, slippery surfaces with special step-like structures were fabricated with the same technological process. Compared with the SA_{up} of TASSs with step-like grooves (*e.g.*, Figure 3d), the single step structure without a back wall showed much smaller SA (Figure S8b, Supporting Information), indicating that the adhesion force from the steps was not the leading source of the tridirectional anisotropy. In addition, it was observed that the step-like grooves (*N*g: 1-4) underlying the droplet had little influence on the SAs (Figure S8a, Supporting Information). Therefore, the single step structure with a back wall was employed to study the influence of adhesion force and pinning on sliding resistance. As depicted in Figure 4a, four sliding configurations could be defined in the "up" and "down" directions according to the main resistance source (*i.e.*, adhesion force from the step and/or back wall, pinning by the step edge), and the corresponding SAs (*i.e.*, $SA_{up\text{-}A}$, $SA_{up\text{-}P}$, $SA_{down\text{-}A}$ and $SA_{down\text{-}P}$, the new subscript "A" and "P" here referred to the droplet adhered to the step and pinned to the step edge, respectively) were measured and shown in Figure 4b. It could be seen that the SAs of all the motion configurations increased with the SN (*i.e.*, the height of the step). When the step height was small (SN = 10), $SA_{up\text{-}A} \approx SA_{up\text{-}P}$, $SA_{down\text{-}A} \approx SA_{down\text{-}P}$, indicating that the adhesion force was almost equal to the pinning force in both "up" and "down" directions. However, as the step height increased, the $SA_{up\text{-}P}$ and $SA_{down\text{-}P}$ grew rapidly while $SA_{up\text{-}A}$ and $SA_{down\text{-}A}$ increased slowly, which demonstrated that the pinning effect by the step edge contributed more to the sliding resistance than the adhesion force. When SN = 50, the droplet was even completely pinned at the edge during sliding towards the "up" direction (*i.e.*, $SA_{up\text{-}P} = 90°$). Therefore, it could be inferred that the $F_{resistance}$ of droplet sliding on the

TASS was mainly determined by the pinning force at the step edge. Meanwhile, the difference between $SA_{up\text{-}A}$ and $SA_{down\text{-}A}$ was negligible, indicating that the introduction of the step structure had little influence on the adhesion force between the slippery surface and droplet. Nevertheless, the $SA_{up\text{-}P}$ was much larger than $SA_{down\text{-}P}$, which suggested that the pinning force on the droplet sliding in the "up" direction was larger than that in the "down" direction. These results were consistent with the measured SAs on the TASS (*e.g.*, Figure 3d), and revealed that the pinning effect at the step edge was critical to the tridirectionally anisotropic sliding of the droplet on the TASS.

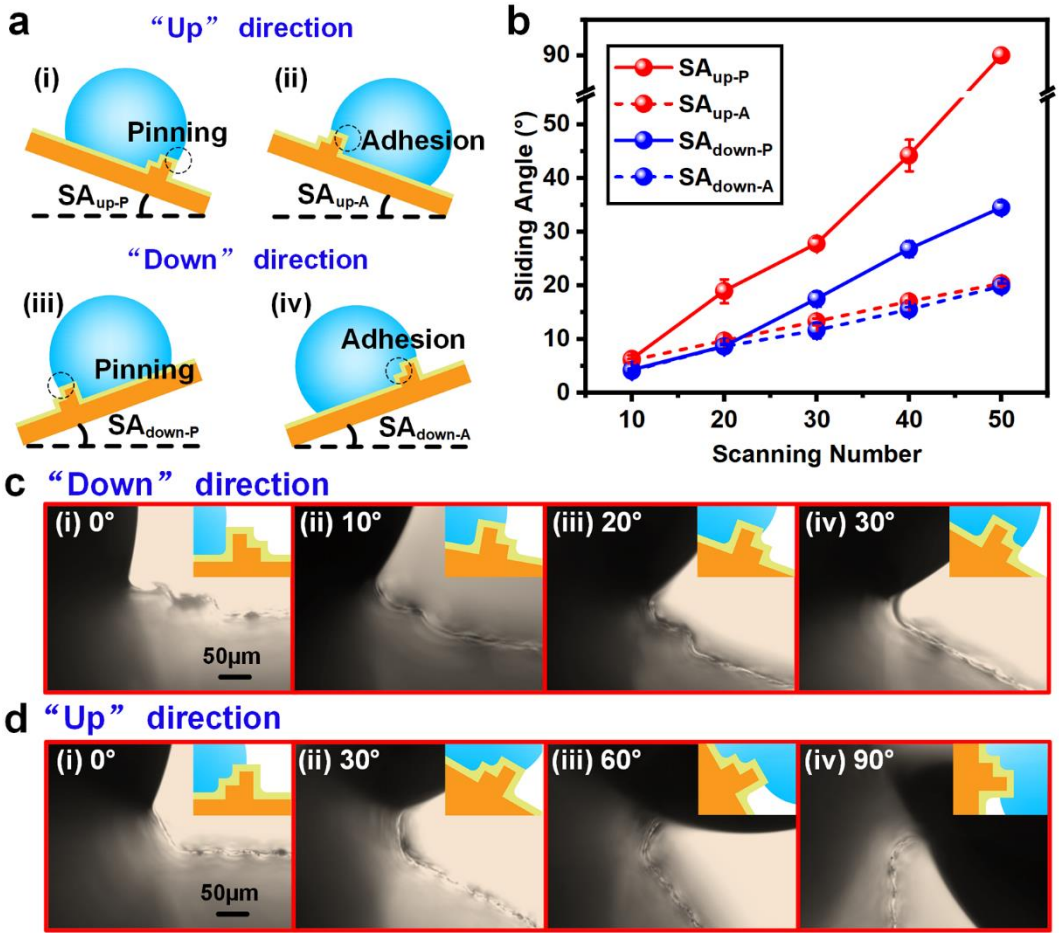

Figure 4. a) Schematic illustration of four configurations of water droplet sliding on slippery surface with a single step structure with back wall and b) their corresponding SAs. The pinned states of water droplet at different tilting angles in the c) "down" direction and d) "up" direction.

To demonstrate the pinning effect of the step edge visually, digital images showing droplet sliding

in “up” and “down” directions around the step edge (SN = 50) were captured and presented in Figure 4c and d. In the “down” direction (Figure 4c), when the tilting angle of the surface was gradually increased from 0° to 10°, the droplet was firstly pinned at the step edge (Figure 4c (ii)), which resulted in the increase of advancing CA as the tilting angle was increased to 20° (Figure 4c (iii)). When the tilting angle was further increased to 30° (Figure 4c (iv)), the wetting ridge around the base of the droplet made contact with the wetting ridge at the corner of the step, which was similar to the phenomenon of the Cheerios effect [67], [68]. Finally, the droplet moved downward and then slid across the top edge of the step with the assistance of gravity. By contrast, in the “up” direction (Figure 4d), the droplet slowly moved forward on the top surface of the step as the tilting angle was increased, but it was tightly pinned at the step edge even when the tilting angle was 60° (Figure 4d (iii)). Although the advancing CA continuously increased and the wetting ridge slightly moved down along the back wall when the tilting angle was 90° (Figure 4d (iv)), the droplet could not contact with the bottom of the surface along the back wall, which finally stopped the sliding of the droplet. Consequently, the movement of the droplet was significantly influenced by the pinning effect of the step edge and the height of the step walls (*i.e.*, h_1 and h_2 in Figure 2d). Owing to the fact that $h_2 \approx 2h_1$, sliding in the “up” direction required a larger tilting angle than that in the “down” direction, resulting in the anisotropic sliding between the “up” and “down” directions on the TASS.

3.5 Horizontal Unidirectional Transport of Droplet

The as-prepared TASS possessed rice-leaf-like unidirectional sliding capacity in the “//” direction, as well as butterfly-wing-like property of anisotropic droplet manipulation in the “up” and “down” directions, enabling the TASS to be capable of transporting droplet unidirectionally. As shown in Figure S9a and Video S2 (Supporting Information), when water was continuously injected onto the TASS via a syringe, unidirectional spreading occurred in the “⊥” direction and the droplet could only

advance towards the “down” direction, but it spread uniformly in the “//” direction, which corresponded well with the anisotropic wettability of the TASS. Taking advantage of such a unidirectional spreading of a droplet on TASS, two TASSs with the same step direction were placed face-to-face to squeeze a water droplet that was pre-deposited in between them to realize continuous unidirectional transport. As shown in Figure S9b and Video S3 (Supporting Information), when the upper TASS moved downward, the droplet was squeezed and then deformed, owing to the pinning effect in the “up” direction originating from both upper and lower TASSs, the droplet deformation only propagated towards the “down” direction. When the upper TASS was withdrawn, the droplet tended to recover its original shape, during which the droplet movement was obstructed by the adhesion forces from both “up” and “down” directions of the two TASSs. However, the adhesion forces were roughly equal and rather small, enabling the contact lines in the two directions to move towards the middle position of the deformed droplet uniformly. Finally, unidirectional movement of the droplet towards the “down” direction of the TASS was thereby observed. By repeating the squeezing process, continuous transport of the droplet could be realized. By contrast, when the step direction of the upper TASS was opposite to the lower TASS, the squeezed droplet tended to spread uniformly towards the “up” and “down” directions (Figure S9c and Video S3, Supporting Information), which could be attributed to the equal but direction-opposite pinning forces applied on the droplet. Therefore, the droplet would not be transported in this case.

As mentioned above, the deformation of the droplet and unbalanced force acting on the contact lines could favor a unidirectional movement of the droplet on the TASS. Therefore, mechanical vertical vibration was applied on the TASS so as to trigger the deformation of the droplet and then promote its rapid and unidirectional transport by utilizing the pinning effect from the step edge (Figure 5a). As an example, Figure 5b and Video S4 (Supporting Information) show the unidirectional

transport of a water droplet (7 μL) under the assistance of vertical vibration with a frequency of 50 Hz and vibration amplitude of 3 Vpp. It can be seen that the water droplet is transporting unidirectionally with a speed of ≈2.7 mm/s under this vertical vibration. In addition, the unidirectional transport of glycol droplet was also demonstrated (Video S5, Supporting Information), but the speed was relatively low (≈0.5 mm/s) due to its high viscosity that seriously delayed the deformation and spreading of the droplet during vibration excitation. By contrast, on a slippery surface with rice-leaf-like micro grooves (*i.e.*, no steps existed in the grooves), the droplet deformed but could not be transported under vertical vibration driving (Video S6, Supporting Information), which also highlighted the indispensable role of the step-like structures in terms of unidirectional droplet transport in our design. Moreover, integrated TASSs with step-to-step structures (Figure 5c) and back-to-back structures (Figure 5d) were designed to regulate the transport direction of two droplets on the same TASS. By using such layouts of the step-like micro structures, rapid merging (Figure 5c and Video S7 (Supporting Information)) and separation (Figure 5d and Video S8 (Supporting Information)) of two droplets were realized under the assistance of vertical vibration.

Next, several factors which potential influence the U_{CA} were investigated. As shown in Figure S10 and S11 (Supporting Information), the U_{CA} could be roughly controlled by adjusting the height (*i.e.*, SN) and period of the step-like micro grooves, and it was also found that the U_{CA} always decreased when the excitation frequency increased from 30 Hz to 50 Hz. This was due to high-frequency vibration accelerating the deforming of the droplet and increasing the radial length of the deformed droplet, which thereby triggered the movement of the droplet towards the “down” direction on TASS under a relatively low vibration amplitude. By using the SN-dependent U_{CA}, a groove-features controlled chemical micro reactor was designed and illustrated in Figure 5e. TASS with two areas composed of different step-like micro grooves (the corresponding SNs were respectively 20 and 30)

were arranged with a step-to-step layout. As shown in Figure 5g and video S10 (Supporting Information), based on the different U_{CA} for droplets on the TASS with various SNs, when the vibration frequency was 50 Hz and the vibration amplitude was set to be 3.0 Vpp, the $CuCl_2$ droplet (7 μL) pre-deposited at the left part of the TASS (SN = 20) was transported along the "down" direction and pinned at the middle section, while the NaOH droplet (7 μL) at the right part stayed at the original position. After increasing the vibration amplitude to 3.6 Vpp, the NaOH droplet started to move and then merged with the $CuCl_2$ droplet, which finally led to the formation $Cu(OH)_2$ precipitate.

In addition, Figure S12 (Supporting Information) depicted the relationship between U_{CA} and the volume of droplets. It could be seen that micro water droplet with the smallest volume of 1.4 μL could be transported on the TASS under the assistance of vibration with a frequency of 50 Hz and amplitude of 7.2 Vpp. At the frequency of 30 Hz, the U_{CA} decreased continuously when the volume of the droplet increased from 2.5 μL to 50 μL. By contrast, when the frequency was increased to 40 Hz or 50 Hz, the U_{CA} initially decreased sharply and then increased slightly as the volume increased, and the lowest U_{CA} at the frequency of 40 Hz and 50 Hz were respectively 1.6 Vpp and 2.3 Vpp, and the corresponding volumes of droplet were 20 μL and 15 μL, respectively. Moreover, when the volume of droplet was too large, it could not be effectively transported on the TASS because obvious droplet splashing occurred under vibration excitation, as shown in Figure S13 and Video S9 (Supporting Information). According to the volume-dependent U_{CA} of the TASS, a chemical micro-reactor based on two droplets with different volumes was demonstrated. As illustrated in Figure 5f, two areas of micro grooves with the same SN of 20 were arranged to be step-to-step to construct the demanded TASS, and $CuCl_2$ droplet with a volume of 10 μL and NaOH droplet with a volume of 7 μL were respectively deposited on the left and right areas of the TASS. As shown in Figure 7h and Video S11

(Supporting Information), the $CuCl_2$ droplet (10 μL) and NaOH droplet (7 μL) started to move towards the middle position of the TASS when the amplitude of the vibration (frequency of 50 Hz) was respectively set to 2.4 Vpp and 3.0 Vpp, which finally triggered the droplet-based micro reaction between $CuCl_2$ and NaOH.

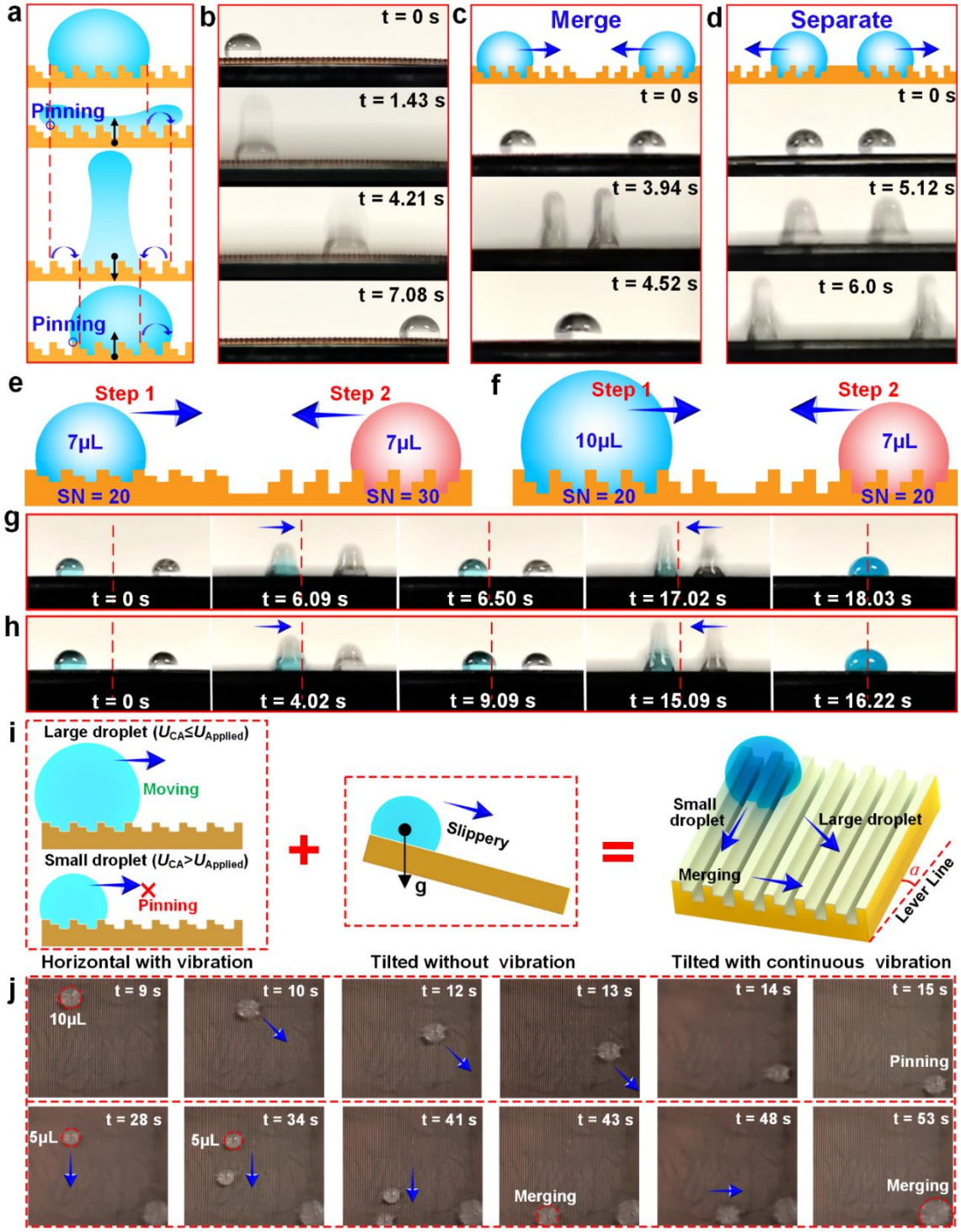

Figure 5. Vibration-driven programmable transport of droplets on TASS. a) Schematic diagram of the deformation

and movement of a droplet under vertical vibration excitation. The black arrows represented the vibration direction, and the blue arrows indicated the contact line movement direction. b) Unidirectional transport of a 7 μL water droplet under vertical vibration with a frequency of 50 Hz and vibration amplitude of 3 Vpp. c) Merging and d) separation of droplets on step-to-step and back-to-back TASSs, respectively. Schematic diagram of e) SN- and f) volume-based unidirectional transport of droplets. Digital images showing vibration-driven sequential and unidirectional transport of g) droplets on TASS with different SNs and h) droplets with different volumes. i) Schematic diagram of programmable droplet transport on tilted TASS under vertical vibration driving. j) Time-lapse photographs of programmable transport of droplets with different volumes on tilted TASS.

Furthermore, a tilted TASS was used to realize programmable droplet transport under vibration assistance by using the tridirectionally anisotropic wettability. For a certainly applied vibration amplitude ($U_{Applied}$) that was higher than the U_{CA} of a large droplet but lower than that of a small droplet (Figure S12, Supporting Information), it could drive the movement of the large droplet along the "down" direction of the horizontal TASS but pinned the small droplet. Meanwhile, the droplet on a tilted TASS tended to slide along the "//" direction of the micro grooves under the assistance of gravity. Therefore, as illustrated in Figure 5i, by combining the $U_{Applied}$-controlled selective transport along the "down" direction and gravity-driven sliding along the "//" direction, a TASS-based platform for programmable droplet transport could be designed. As shown in Figure 5j and Video S12 (Supporting Information), a TASS was tilted at 1° along the "//" direction, and vibration with a frequency of 50 Hz and amplitude of 2.4 Vpp was continuously applied. When a droplet with a volume of 10 μL (U_{CA} = 2.4 Vpp) was deposited on the TASS, transport along both "//" and "down" directions occurred, which synthesized a sliding along the diagonal direction of the substrate, and the droplet was then pinned at the corner. However, when two droplets with a volume of 5 μL

(U_{CA} = 3.7 Vpp) were dropped on the TASS, they could not move along the "down" direction but only slid along the "//" direction. After they were pinned and merged at the margin of the substrate, a new droplet with a volume of 10 μL was formed, which met the requirement of vibration-assisted unidirectional transport along the "down" direction (*i.e.*, $U_{Applied} \geq U_{CA}$) on the TASS. Due to the confinement of the margin, the formed droplet was transported along the "down" direction and finally merged with the droplet that was pre-located at the corner. Therefore, the TASS could be used as a versatile and multifunctional platform for programmable droplet transport.

4. Conclusion

In conclusion, inspired by the wettability of rice leaf, butterfly wing, and Pitcher plant, a multi-bionic TASS with step-like grooves was prepared to manipulate liquid droplet in three directions. The Pitcher plant-like slipperiness enabled ultra-easy sliding for droplet along the direction that was parallel to grooves (*i.e.*, the "//" direction), while the pinning effect at the corner boundaries of the steps resulted in anisotropic sliding in the two opposite directions that were perpendicular to the grooves (termed as the "up" and "down" directions). It was also demonstrated that the height and period of the steps had an obvious influence on the magnitude of the anisotropy between the "up" and "down" directions. The tridirectional anisotropy allowed unidirectional droplet motion on horizontally placed TASS under the assistance of vertical vibration, and the motion could be manipulated *via* controlling the features of the grooves, the volume of the droplet, and the frequency of the vibration. Based on the excellent tridirectional anisotropy, programmable droplet transports, such as merging and separation of droplets, sequential droplet-based chemical micro-reactions, and synthetic motion of droplets, were demonstrated on specially designed TASSs. The multi-bioinspired TASS thereby provides new insights into the development of functional surfaces with special wettability for droplet manipulation, as well as a new platform for lab-on-chip systems, chemical

reactors, *etc*.

Acknowledgement

This work was financially supported by the National Postdoctoral Program for Innovative Talents (No. BX20190233), National Natural Science Foundation of China (No. 52105477, 22075202), and the Open Project Program of Key Laboratory for Cross-Scale Micro and Nano Manufacturing of Ministry of Education, Changchun University of Science and Technology (No. CMNM-KF202102).

References

[1] Y. Zheng, H. Bai, Z. Huang, X. Tian, F.-Q. Nie, Y. Zhao, J. Zhai, L. Jiang, Directional water collection on wetted spider silk, Nature 463(7281) (2010) 640-643. https://doi.org/10.1038/nature08729.

[2] M. Liu, S. Wang, L. Jiang, Nature-inspired superwettability systems, Nature Reviews Materials 2(7) (2017) 17036. https://doi.org/10.1038/natrevmats.2017.36.

[3] K.-C. Park, P. Kim, A. Grinthal, N. He, D. Fox, J.C. Weaver, J. Aizenberg, Condensation on slippery asymmetric bumps, Nature 531(7592) (2016) 78-82. https://doi.org/10.1038/nature16956.

[4] P. Zhu, R. Chen, C. Zhou, Y. Tian, L. Wang, Asymmetric fibers for efficient fog harvesting, Chemical Engineering Journal 415 (2021) 128944. https://doi.org/10.1016/j.cej.2021.128944.

[5] S. Jiang, Y. Hu, H. Wu, R. Li, Y. Zhang, C. Chen, C. Xue, B. Xu, W. Zhu, J. Li, D. Wu, J. Chu, Three-Dimensional Multifunctional Magnetically Responsive Liquid Manipulator Fabricated by Femtosecond Laser Writing and Soft Transfer, Nano Letters 20(10) (2020) 7519-7529. https://doi.org/10.1021/acs.nanolett.0c02997.

[6] Q. Zhang, G. Gao, G. Lu, L. Shao, F. Shi, L. Jiang, M. Cheng, Superhydrophobic coating modified nozzles for energy-saving rapid micro-mixing, Chemical Engineering Journal 419 (2021) 129766. https://doi.org/10.1016/j.cej.2021.129766.

[7] L. Fang, J. Zhang, Y. Chen, S. Liu, Q. Chen, A. Ke, L. Duan, S. Huang, X. Tian, Z. Xie, High-Resolution

Patterned Functionalization of Slippery “Liquid-Like” Brush Surfaces via Microdroplet-Confined Growth of Multifunctional Polydopamine Arrays, Advanced Functional Materials 31(19) (2021) 2100447. https://doi.org/10.1002/adfm.202100447.

[8] J.Y. Lu, F.R. Zhang, X.Z. Ding, L.Q. Xia, W.T. Huang, Natural interface guiding cell: Directly using waste fish scales with rich micro/nano structures for control of cell behaviors, Applied Surface Science 581 (2022) 152348. https://doi.org/10.1016/j.apsusc.2021.152348.

[9] B. Yi, H. Zhang, Z. Yu, H. Yuan, X. Wang, Y. Zhang, Fabrication of high performance silk fibroin fibers via stable jet electrospinning for potential use in anisotropic tissue regeneration, Journal of Materials Chemistry B 6(23) (2018) 3934-3945. https://doi.org/10.1039/C8TB00535D.

[10] H. Zhang, C. Chen, H. Zhang, G. Chen, Y. Wang, Y. Zhao, Janus medical sponge dressings with anisotropic wettability for wound healing, Applied Materials Today 23 (2021) 101068. https://doi.org/10.1016/j.apmt.2021.101068.

[11] Y. Hirai, H. Mayama, Y. Matsuo, M. Shimomura, Uphill Water Transport on a Wettability-Patterned Surface: Experimental and Theoretical Results, ACS Applied Materials & Interfaces 9(18) (2017) 15814-15821. https://doi.org/10.1021/acsami.7b00806.

[12] K. Yin, S. Yang, X. Dong, D. Chu, J.-A. Duan, J. He, Ultrafast Achievement of a Superhydrophilic/Hydrophobic Janus Foam by Femtosecond Laser Ablation for Directional Water Transport and Efficient Fog Harvesting, ACS Applied Materials & Interfaces 10(37) (2018) 31433-31440. https://doi.org/10.1021/acsami.8b11894.

[13] J. Wu, K. Yin, M. Li, Z. Wu, S. Xiao, H. Wang, J.-A. Duan, J. He, Under-oil self-driven and directional transport of water on a femtosecond laser-processed superhydrophilic geometry-gradient structure, Nanoscale 12(6) (2020) 4077-4084. https://doi.org/10.1039/C9NR09902F.

[14] X. Wang, J. Zeng, J. Li, X. Yu, Z. Wang, Y. Zhang, Beetle and cactus-inspired surface endows continuous

and directional droplet jumping for efficient water harvesting, Journal of Materials Chemistry A 9(3) (2021) 1507-1516. https://doi.org/10.1039/D0TA10123K.

[15] Y.-Q. Luo, F. Song, C. Xu, X.-L. Wang, Y.-Z. Wang, Bioinspired fabrication of asymmetric wood materials for directional liquid manipulation and transport, Chemical Engineering Journal 383 (2020) 123168. https://doi.org/10.1016/j.cej.2019.123168.

[16] Z. Yu, T. Zhu, J. Zhang, M. Ge, S. Fu, Y. Lai, Fog Harvesting Devices Inspired from Single to Multiple Creatures: Current Progress and Future Perspective, Advanced Functional Materials (2022). https://doi.org/10.1002/adfm.202200359.

[17] S. Huang, J. Li, L. Liu, L. Zhou, X. Tian, Lossless Fast Drop Self-Transport on Anisotropic Omniphobic Surfaces: Origin and Elimination of Microscopic Liquid Residue, Advanced Materials 31(27) (2019) 1901417. https://doi.org/10.1002/adma.201901417.

[18] J. Jiang, J. Gao, H. Zhang, W. He, J. Zhang, D. Daniel, X. Yao, Directional pumping of water and oil microdroplets on slippery surface, Proceedings of the National Academy of Sciences 116(7) (2019) 2482-2487. https://doi.org/10.1073/pnas.1817172116.

[19] X. Zhang, L. Sun, Y. Wang, F. Bian, Y. Wang, Y. Zhao, Multibioinspired slippery surfaces with wettable bump arrays for droplets pumping, Proceedings of the National Academy of Sciences 116(42) (2019) 20863-20868. https://doi.org/10.1073/pnas.1912467116.

[20] B. Tang, C. Meng, L. Zhuang, J. Groenewold, Y. Qian, Z. Sun, X. Liu, J. Gao, G. Zhou, Field-Induced Wettability Gradients for No-Loss Transport of Oil Droplets on Slippery Surfaces, ACS Applied Materials & Interfaces 12(34) (2020) 38723-38729. https://doi.org/10.1021/acsami.0c06389.

[21] M. Sindoro, S. Granick, Ionic Janus Liquid Droplets Assembled and Propelled by Electric Field, Angewandte Chemie International Edition 57(51) (2018) 16773-16776. https://doi.org/10.1002/anie.201810862.

562 [22] N. Miljkovic, D.J. Preston, R. Enright, E.N. Wang, Electrostatic charging of jumping droplets, Nature
563 Communications 4(1) (2013) 2517. https://doi.org/10.1038/ncomms3517.
564 [23] S. Feng, Q. Wang, Y. Xing, Y. He, X. Geng, Y. Hou, Y. Zheng, Electromigration-triggered programmable
565 droplet spreading, Chemical Engineering Journal 423 (2021) 130281.
566 https://doi.org/10.1016/j.cej.2021.130281.
567 [24] J. Li, Y. Hou, Y. Liu, C. Hao, M. Li, M.K. Chaudhury, S. Yao, Z. Wang, Directional transport of high-
568 temperature Janus droplets mediated by structural topography, Nature Physics 12(6) (2016) 606-612.
569 https://doi.org/10.1038/nphys3643.
570 [25] A. Bouillant, T. Mouterde, P. Bourrianne, A. Lagarde, C. Clanet, D. Quéré, Leidenfrost wheels, Nature
571 Physics 14(12) (2018) 1188-1192. https://doi.org/10.1038/s41567-018-0275-9.
572 [26] Z. Wu, K. Yin, J. Wu, Z. Zhu, J.-A. Duan, J. He, Water droplet rapid spreading transport on femtosecond
573 laser-treated photothermal and superhydrophilic surface, Optics & Laser Technology 141 (2021) 107099.
574 https://doi.org/10.1016/j.optlastec.2021.107099.
575 [27] A. Li, H. Li, Z. Li, Z. Zhao, K. Li, M. Li, Y. Song, Programmable droplet manipulation by a magnetic-
576 actuated robot, Science Advances 6(7) (2020) eaay5808. https://doi.org/doi:10.1126/sciadv.aay5808.
577 [28] W. Chen, X. Zhang, S. Zhao, J. Huang, Z. Guo, Slippery magnetic track inducing droplet and bubble
578 manipulation, Chemical communications 58(8) (2022) 1207-1210. https://doi.org/10.1039/d1cc06369c.
579 [29] Y. Fang, J. Liang, X. Bai, J. Yong, J. Huo, Q. Yang, X. Hou, F. Chen, Magnetically Controllable
580 Isotropic/Anisotropic Slippery Surface for Flexible Droplet Manipulation, Langmuir 36(50) (2020) 15403-
581 15409. https://doi.org/10.1021/acs.langmuir.0c03008.
582 [30] J. Wang, Z. Zhu, P. Liu, S. Yi, L. Peng, Z. Yang, X. Tian, L. Jiang, Magneto-Responsive Shutter for On-
583 Demand Droplet Manipulation, Advanced Science 8(23) (2021) 2103182.
584 https://doi.org/10.1002/advs.202103182.

585 [31] Y. Zhang, J. Li, L. Xiang, J. Wang, T. Wu, Y. Jiao, S. Jiang, C. Li, S. Fan, J. Zhang, H. Wu, Y. Zhang, Y.
586 Bian, K. Zhao, Y. Peng, W. Zhu, J. Li, Y. Hu, D. Wu, J. Chu, Z. Wang, A Biocompatible Vibration-Actuated
587 Omni-Droplets Rectifier with Large Volume Range Fabricated by Femtosecond Laser, Advanced Materials
588 34(12) (2022) 2108567. https://doi.org/10.1002/adma.202108567.
589 [32] D. Wu, Z. Zhang, Y. Zhang, Y. Jiao, S. Jiang, H. Wu, C. Li, C. Zhang, J. Li, Y. Hu, G. Li, J. Chu, L. Jiang,
590 High-Performance Unidirectional Manipulation of Microdroplets by Horizontal Vibration on Femtosecond
591 Laser-Induced Slant Microwall Arrays, Advanced Materials 32(48) (2020) 2005039.
592 https://doi.org/10.1002/adma.202005039.
593 [33] T.A. Duncombe, E.Y. Erdem, A. Shastry, R. Baskaran, K.F. Böhringer, Controlling Liquid Drops with
594 Texture Ratchets, Advanced Materials 24(12) (2012) 1545-1550. https://doi.org/10.1002/adma.201104446.
595 [34] H.R. Holmes, K.F. Böhringer, Transport velocity of droplets on ratchet conveyors, Advances in Colloid
596 and Interface Science 255 (2018) 18-25. https://doi.org/10.1016/j.cis.2017.08.009.
597 [35] L. Feng, S. Li, Y. Li, H. Li, L. Zhang, J. Zhai, Y. Song, B. Liu, L. Jiang, D. Zhu, Super-Hydrophobic
598 Surfaces: From Natural to Artificial, Advanced Materials 14(24) (2002) 1857-1860.
599 https://doi.org/10.1002/adma.200290020.
600 [36] X. Luo, H. Lai, Z. Cheng, P. Liu, Y. Li, X. Yu, Y. Liu, Slippery shape memory polymer arrays with
601 switchable isotropy/anisotropy and its application as a reprogrammable platform for controllable droplet
602 motion, Chemical Engineering Journal 403 (2021) 126356. https://doi.org/10.1016/j.cej.2020.126356.
603 [37] Y. Fang, J. Yong, F. Chen, J. Huo, Q. Yang, J. Zhang, X. Hou, Bioinspired Fabrication of
604 Bi/Tridirectionally Anisotropic Sliding Superhydrophobic PDMS Surfaces by Femtosecond Laser, Advanced
605 Materials Interfaces 5(6) (2018) 1701245. https://doi.org/10.1002/admi.201701245.
606 [38] S. Li, P. Xiao, W. Zhou, Y. Liang, S.-W. Kuo, T. Chen, Bioinspired Nanostructured Superwetting Thin-
607 Films in a Self-supported form Enabled “Miniature Umbrella” for Weather Monitoring and Water Rescue,

608 Nano-Micro Letters 14(1) (2021) 32. https://doi.org/10.1007/s40820-021-00775-4.
609 [39] Z. Chen, Z. Zhang, Y. Wang, D. Xu, Y. Zhao, Butterfly inspired functional materials, Materials Science
610 and Engineering: R: Reports 144 (2021) 100605. https://doi.org/10.1016/j.mser.2020.100605.
611 [40] T.S. Wong, S.H. Kang, S.K. Tang, E.J. Smythe, B.D. Hatton, A. Grinthal, J. Aizenberg, Bioinspired self-
612 repairing slippery surfaces with pressure-stable omniphobicity, Nature 477(7365) (2011) 443-7.
613 https://doi.org/10.1038/nature10447.
614 [41] L. Shang, Y. Yu, W. Gao, Y. Wang, L. Qu, Z. Zhao, R. Chai, Y. Zhao, Bio-Inspired Anisotropic Wettability
615 Surfaces from Dynamic Ferrofluid Assembled Templates, Advanced Functional Materials 28(7) (2018)
616 1705802. https://doi.org/10.1002/adfm.201705802.
617 [42] L. Sun, Y. Wang, X. Zhang, F. Bian, L. Shang, Y. Zhao, W. Sun, Bio-inspired self-replenishing and self-
618 reporting slippery surfaces from colloidal co-assembly templates, Chemical Engineering Journal 426 (2021)
619 131641. https://doi.org/10.1016/j.cej.2021.131641.
620 [43] S. Zhang, J. Huang, Z. Chen, Y. Lai, Bioinspired Special Wettability Surfaces: From Fundamental
621 Research to Water Harvesting Applications, Small 13(3) (2017) 1602992.
622 https://doi.org/10.1002/smll.201602992.
623 [44] J. Xu, Y. Hou, Z. Lian, Z. Yu, Z. Wang, H. Yu, Bio-Inspired Design of Bi/Tridirectionally Anisotropic
624 Sliding Superhydrophobic Titanium Alloy Surfaces, Nanomaterials 10(11) (2020) 2140.
625 https://doi.org/10.3390/nano10112140.
626 [45] X. Bai, Q. Yang, Y. Fang, J. Yong, Y. Bai, J. Zhang, X. Hou, F. Chen, Anisotropic, adhesion-switchable,
627 and thermal-responsive superhydrophobicity on the femtosecond laser-structured shape-memory polymer for
628 droplet manipulation, Chemical Engineering Journal 400 (2020) 125930.
629 https://doi.org/10.1016/j.cej.2020.125930.
630 [46] J. Long, P. Fan, D. Jiang, J. Han, Y. Lin, M. Cai, H. Zhang, M. Zhong, Anisotropic Sliding of Water

631 Droplets on the Superhydrophobic Surfaces with Anisotropic Groove-Like Micro/Nano Structures, Advanced
632 Materials Interfaces 3(24) (2016) 1600641. https://doi.org/10.1002/admi.201600641.
633 [47] X. Liang, Z. Guo, Mechano-adjusted anisotropic surface for manipulating water droplets, Chemical
634 Engineering Journal 395 (2020) 125110. https://doi.org/10.1016/j.cej.2020.125110.
635 [48] W. Wang, J.V.I. Timonen, A. Carlson, D.-M. Drotlef, C.T. Zhang, S. Kolle, A. Grinthal, T.-S. Wong, B.
636 Hatton, S.H. Kang, S. Kennedy, J. Chi, R.T. Blough, M. Sitti, L. Mahadevan, J. Aizenberg, Multifunctional
637 ferrofluid-infused surfaces with reconfigurable multiscale topography, Nature 559(7712) (2018) 77-82.
638 https://doi.org/10.1038/s41586-018-0250-8.
639 [49] X. Gou, Z. Guo, Reed leaf-inspired anisotropic slippery lubricant-infused surface for water collection and
640 bubble transportation, Chemical Engineering Journal 411 (2021). https://doi.org/10.1016/j.cej.2021.128495.
641 [50] M. Soltani, K. Golovin, Lossless, Passive Transportation of Low Surface Tension Liquids Induced by
642 Patterned Omniphobic Liquidlike Polymer Brushes, Advanced Functional Materials 32(1) (2022) 2107465.
643 https://doi.org/10.1002/adfm.202107465.
644 [51] A. Lafuma, D. Quéré, Superhydrophobic states, Nature Materials 2(7) (2003) 457-460.
645 https://doi.org/10.1038/nmat924.
646 [52] X. Dai, N. Sun, S.O. Nielsen, B.B. Stogin, J. Wang, S. Yang, T.-S. Wong, Hydrophilic directional slippery
647 rough surfaces for water harvesting, Science Advances 4(3) (2018) eaaq0919.
648 https://doi.org/doi:10.1126/sciadv.aaq0919.
649 [53] P. Li, M. Cao, H. Bai, T. Zhao, Y. Ning, X. Wang, K. Liu, L. Jiang, Unidirectional Liquid Manipulation
650 Via an Integrated Mesh with Orthogonal Anisotropic Slippery Tracks, Advanced Functional Materials 29(42)
651 (2019). https://doi.org/10.1002/adfm.201904446.
652 [54] X. Yang, K. Zhuang, Y. Lu, X. Wang, Creation of Topological Ultraslippery Surfaces for Droplet Motion
653 Control, ACS Nano 15(2) (2021) 2589-2599. https://doi.org/10.1021/acsnano.0c07417.

[55] J. Chao, J. Feng, F. Chen, B. Wang, Y. Tian, D. Zhang, Fabrication of superamphiphobic surfaces with controllable oil adhesion in air, Colloids and Surfaces A: Physicochemical and Engineering Aspects 610 (2021). https://doi.org/10.1016/j.colsurfa.2020.125708.

[56] X. Dai, B.B. Stogin, S. Yang, T.-S. Wong, Slippery Wenzel State, ACS Nano 9(9) (2015) 9260-9267. https://doi.org/10.1021/acsnano.5b04151.

[57] J. Ma, W. Pan, Y. Li, J. Song, Slippery coating without loss of lubricant, Chemical Engineering Journal 444 (2022) 136606. https://doi.org/10.1016/j.cej.2022.136606.

[58] C. Long, Y. Qing, K. An, X. Long, C. Liu, S. Shang, C. Yang, C. Liu, Functional fluorination agents for opposite extreme wettability coatings with robustness, water splash inhibition, and controllable oil transport, Chemical Engineering Journal 415 (2021) 128895. https://doi.org/10.1016/j.cej.2021.128895.

[59] T. Young, An essay on the cohesion of fluids, Proceedings of the Royal Society of London 1 (1832) 171-172. https://doi.org/10.1098/rspl.1800.0095.

[60] Z. Wang, K. Lin, Y.-P. Zhao, The effect of sharp solid edges on the droplet wettability, Journal of Colloid and Interface Science 552 (2019) 563-571. https://doi.org/10.1016/j.jcis.2019.05.081.

[61] C.-W. Yao, C.-L. Lai, J.L. Alvarado, J. Zhou, K.T. Aung, J.E. Mejia, Experimental study on effect of surface vibration on micro textured surfaces with hydrophobic and hydrophilic materials, Applied Surface Science 412 (2017) 45-51. https://doi.org/10.1016/j.apsusc.2017.03.211.

[62] Y. Yuan, T.R. Lee, Contact Angle and Wetting Properties, in: G. Bracco, B. Holst (Eds.), Surface Science Techniques, Springer Berlin Heidelberg, Berlin, Heidelberg, 2013, pp. 19-20. https://doi.org/10.1007/978-3-642-34243-1_1.

[63] Z. Wang, L. Heng, L. Jiang, Effect of lubricant viscosity on the self-healing properties and electrically driven sliding of droplets on anisotropic slippery surfaces, Journal of Materials Chemistry A 6(8) (2018) 3414-3421. https://doi.org/10.1039/c7ta10439a.

[64] X. Yao, J. Ju, S. Yang, J. Wang, L. Jiang, Temperature-Driven Switching of Water Adhesion on Organogel Surface, Advanced Materials 26(12) (2014) 1895-1900. https://doi.org/10.1002/adma.201304798.

[65] S. Zhang, J. Huang, Y. Cheng, H. Yang, Z. Chen, Y. Lai, Bioinspired Surfaces with Superwettability for Anti-Icing and Ice-Phobic Application: Concept, Mechanism, and Design, Small 13(48) (2017) 1701867. https://doi.org/10.1002/smll.201701867.

[66] T. Guo, P. Che, L. Heng, L. Fan, L. Jiang, Anisotropic Slippery Surfaces: Electric-Driven Smart Control of a Drop's Slide, Advanced Materials 28(32) (2016) 6999-7007. https://doi.org/10.1002/adma.201601239.

[67] A. Gauthier, D. van der Meer, J.H. Snoeijer, G. Lajoinie, Capillary orbits, Nature Communications 10(1) (2019) 3947. https://doi.org/10.1038/s41467-019-11850-1.

[68] A. Jagota, Role reversal: Liquid “Cheerios” on a solid sense each other, Proceedings of the National Academy of Sciences 113(27) (2016) 7294-7295. https://doi.org/10.1073/pnas.1607893113.